



Universiteit
Leiden
The Netherlands

3D-DASH: the widest near-infrared Hubble Space Telescope survey

Mowla, L.A.; Cutler, S.E.; Brammer, G.B.; Momcheva, I.G.; Whitaker, K.E.; Dokkum, P.G. van; ... ; Wel, A. van der

Citation

Mowla, L. A., Cutler, S. E., Brammer, G. B., Momcheva, I. G., Whitaker, K. E., Dokkum, P. G. van, ... Wel, A. van der. (2022). 3D-DASH: the widest near-infrared Hubble Space Telescope survey. *The Astrophysical Journal*, 933(2). doi:10.3847/1538-4357/ac71af

Version: Publisher's Version
License: [Creative Commons CC BY 4.0 license](https://creativecommons.org/licenses/by/4.0/)
Downloaded from: <https://hdl.handle.net/1887/3561288>

Note: To cite this publication please use the final published version (if applicable).



3D-DASH: The Widest Near-infrared Hubble Space Telescope Survey

Lamiya A. Mowla¹ , Sam E. Cutler² , Gabriel B. Brammer^{3,4} , Ivelina G. Momcheva⁵ , Katherine E. Whitaker^{2,3} , Pieter G. van Dokkum⁶ , Rachel S. Bezanson⁷ , Natascha M. Förster Schreiber⁸ , Marijn Franx⁹ , Kartheik G. Iyer¹ , Danilo Marchesini¹⁰ , Adam Muzzin¹¹ , Erica J. Nelson¹² , Rosalind E. Skelton¹³ , Gregory F. Snyder¹⁴ , David A. Wake¹⁵ , Stijn Wuyts¹⁶ , and Arjen van der Wel¹⁷

¹ Dunlap Institute for Astronomy and Astrophysics, University of Toronto, 50 St George St, Toronto, ON M5S 3H4, Canada; lamiya.mowla@utoronto.ca

² Department of Astronomy, University of Massachusetts, Amherst, MA 01003, USA

³ Cosmic Dawn Center (DAWN), Niels Bohr Building Rådmandsgade 62-64 2200 Copenhagen N, Denmark

⁴ Niels Bohr Institute, University of Copenhagen, Lyngbyvej 2, 2100 Copenhagen, Denmark

⁵ Space Telescope Science Institute, Baltimore, MD 21218, USA

⁶ Astronomy Department, Yale University, New Haven, CT 06511, USA

⁷ Department of Physics and Astronomy and PITT PACC, University of Pittsburgh, Pittsburgh, PA 15260, USA

⁸ Max-Planck-Institut für extraterrestrische Physik (MPE), Giessenbachstr. 1, D-85748 Garching, Germany

⁹ Leiden Observatory, P.O. Box 9513, 2300 RA, Leiden, The Netherlands

¹⁰ Department of Physics and Astronomy, Tufts University, Medford, MA, USA

¹¹ Department of Physics and Astronomy, York University, 4700 Keele St, Toronto, Ontario, ON MJ3 1P3, Canada

¹² Department for Astrophysical and Planetary Science, University of Colorado, Boulder, CO 80309, USA

¹³ South African Astronomical Observatory, P.O. Box 9, Observatory 7935, South Africa

¹⁴ Space Telescope Science Institute, 3700 San Martin Dr, Baltimore, MD, 21218, USA

¹⁵ Department of Physics and Astronomy, University of North Carolina Asheville, Asheville, NC 28804, USA

¹⁶ Department of Physics, University of Bath, Claverton Down, Bath BA2 7AY, UK

¹⁷ Sterrenkundig Observatorium, Universiteit Gent, Krijgslaan 281 S9, B-9000 Gent, Belgium

Received 2022 March 30; revised 2022 May 10; accepted 2022 May 18; published 2022 July 8

Abstract

The 3D-Drift And SHift (3D-DASH) program is a Hubble Space Telescope (HST) WFC3 F160W imaging and G141 grism survey of the equatorial COSMOS field. 3D-DASH extends the legacy of HST near-infrared imaging and spectroscopy to degree-scale swaths of the sky, enabling the identification and study of distant galaxies ($z > 2$) that are rare or in short-lived phases of galaxy evolution at rest-frame optical wavelengths. Furthermore, when combined with existing ACS/F814W imaging, the program facilitates spatially resolved studies of the stellar populations and dust content of intermediate redshift ($0.5 < z < 2$) galaxies. Here we present the reduced F160W imaging mosaic available to the community. Observed with the efficient DASH technique, the mosaic comprises 1256 individual WFC3 pointings, corresponding to an area of 1.35 deg^2 (1.43 deg^2 in 1912 when including archival data). The median 5σ point-source limit in H_{160} is $24.74 \pm 0.20 \text{ mag}$. We also provide a point-spread function (PSF) generator tool to determine the PSF at any location within the 3D-DASH footprint. 3D-DASH is the widest HST/WFC3 imaging survey in the F160W filter to date, increasing the existing extragalactic survey area in the near-infrared at HST resolution by an order of magnitude.

Unified Astronomy Thesaurus concepts: [High-redshift galaxies \(734\)](#); [Galaxy evolution \(594\)](#); [Near infrared astronomy \(1093\)](#); [Sky surveys \(1464\)](#)

1. Introduction

Wide-field near-infrared (NIR) surveys have proven invaluable for the study of the high-mass end of the galaxy stellar mass function at $z > 1$ (where rest-frame optical emission shifts into the NIR) and for determining the prevalence of short-lived events such as mergers, the properties and demographics of active galactic nuclei (AGNs), and the evolution of galaxy groups and clusters. Such surveys have been undertaken from the ground (e.g., NMBS Whitaker et al. 2011, UltraVISTA McCracken et al. 2012; Muzzin et al. 2013, UKIDSS-UDS Lawrence et al. 2007; Williams et al. 2009), but so far not with the Hubble Space Telescope (HST).

Until recently, the largest area imaged with HST in the NIR (J_{125} and H_{160}) was the 0.2 deg^2 Cosmic Assembly Near-infrared Deep Extragalactic Legacy Survey (CANDELS, 900

orbits; Grogin et al. 2011; Koekemoer et al. 2011). “Classical” HST NIR surveys over larger areas have not been executed owing to the fact that a guide star acquisition is required for each new Wide Field Camera 3 (WFC3) pointing. In practice, this sets the minimum exposure time to 1 orbit per pointing, and this means that very large allocations are needed to cover substantial ($>0.5 \text{ deg}^2$) areas. This situation changed with the development and implementation of the Drift And SHift technique (Momcheva et al. 2017), which enables up to eight pointings to be observed within a single orbit (see Section 2.1). This technique allows for an order of magnitude increase in the efficiency of large-area mapping with HST.

The obvious field for a wide-area HST survey in the NIR is the ACS COSMOS field (640 orbits; Scoville et al. 2007; Koekemoer et al. 2007) covering 1.7 degrees^2 ; 15 yr after its execution, this is still the most comprehensive and widest tier of the “wedding cake” of extragalactic survey fields. COSMOS is the ultimate field to study rare objects such as the most massive galaxies (Hill et al. 2017; Mowla et al. 2019b; Marsan et al. 2019; Cooke et al. 2019), close pairs (Xu et al. 2012),



Original content from this work may be used under the terms of the [Creative Commons Attribution 4.0 licence](#). Any further distribution of this work must maintain attribution to the author(s) and the title of the work, journal citation and DOI.

overdense structures (Chiang et al. 2014; Iovino et al. 2016), AGN (Civano et al. 2012), poststarburst galaxies (Whitaker et al. 2012a), etc. The field has exquisite ancillary data ranging from X-rays (e.g., Civano et al. 2016; Marchesi et al. 2016), to submillimeter (e.g., Faisst et al. 2020; Le Fèvre et al. 2020), radio (e.g., Fernández et al. 2016), and in spectroscopy (e.g., van der Wel et al. 2016). It has provided the best constraints that we currently have on the evolution of the galaxy stellar mass function (Muzzin et al. 2013), the evolution of the star formation rates of galaxies (Scoville et al. 2013; Lee et al. 2015), and the evolution of their sizes (Sargent et al. 2007). However, all these measurements suffer from biases as the field lacks high-resolution NIR imaging.

In HST Cycle 23 we obtained pilot DASH observations in a section of the COSMOS field, using 57 orbits to cover 0.49 deg^2 . Several scientific results validated the success of the DASH technique. The COSMOS-DASH image extended the parameter space probed for the galaxy size–mass relation and found that there is no significant difference between the sizes of star-forming and quiescent galaxies at the high-mass end (Mowla et al. 2019b), the size–mass relation of all galaxies can be described by a broken power law with a pivot that is reminiscent of the stellar mass–halo mass relation of galaxies (Mowla et al. 2019a), and that there is a flattening of the quiescent size–mass relation at lower stellar masses (Nedkova et al. 2021; Cutler et al. 2022). COSMOS-DASH has also been used to find early universe massive galaxy candidates (Marsan et al. 2022), which will be of particular importance during the James Webb Space Telescope era.

3D-DASH increases coverage to the entire ACS COSMOS field with both imaging and spectroscopy, thus extending the legacy of HST into the regime of degree-scale NIR imaging and spectroscopy. Combining the pilot program with new data taken in Cycles 23 and 28, the ACS COSMOS field now has coverage in both WFC3/F160W and WFC3/G141, widening the shallow base of the extragalactic wedding cake (Figure 1 and Table 1). 3D-DASH covers 1.35 deg^2 of the COSMOS field down to a median depth of $H_{160} = 24.72 \pm 0.17$ or 1.43 deg^2 down to $H_{160} = 24.74 \pm 0.20$ when ancillary data are included, increasing the extragalactic survey area observed by HST in the NIR by an order of magnitude. This paper presents the F160W imaging of this program (Figures 2 and 3), while a forthcoming paper will present the grism spectroscopy (Figure 4).

The paper is structured as follows: in Section 2 we give a description of the 3D-DASH survey, Section 3 describes the image processing, Section 4 highlights the potential of the data with three examples of science applications, and Section 5 gives a summary of the paper. We assume a Λ CDM cosmology with $\Omega_m = 0.3$, $\Omega_\Lambda = 0.7$, and $H_0 = 70 \text{ km s}^{-1} \text{ Mpc}^{-1}$. The AB magnitude system (Oke & Gunn 1983) is adopted throughout the paper; a Chabrier (2003) initial mass function is used when appropriate.

2. The 3D-DASH Program

2.1. Drift And SHift (DASH)

Drift And SHift (DASH) is an efficient technique to cover an extensive area using the NIR channel of Wide Field Camera 3 (WFC3) on the Hubble Space Telescope (Momcheva et al. 2017). In standard HST observations, guide stars are acquired for each new pointing. Acquiring a guide star takes

approximately 10 minutes, which means that short exposures are only possible with huge overheads. This limits the total number of pointings that can be obtained within an orbit’s visibility window.¹⁸

The guide star acquisition limitation can be circumvented by acquiring a guide star for only the first pointing of an orbit and guiding with the three HST gyros for the remainder. This technique makes it possible to observe up to 8 WFC3 pointings in a single orbit, significantly increasing HST’s large-scale mapping capabilities. Successfully used for the first time in the COSMOS-DASH survey (Mowla et al. 2019b) to image 0.49 deg^2 of the three stripes of the UltraVISTA field (McCracken et al. 2012), DASH remains the most efficient method for wide-area observations with WFC3.

During a standard guided exposure, the three HST gyros receive continuous corrections from the Fine Guidance Sensors (FGS). Turning off guiding stops the stream of corrections from the FGS, and the telescope begins to drift with an expected rate of $0''.001 - 0''.002$ per second. In CCDs, this would lead to detrimental smearing of the image in a typical 5-minute exposure. However, the WFC3/IR detector can perform multiple nondestructive, zero overhead reads throughout the exposure. Setting the time between reads to 25 s or less lowers the drift between reads to $\leq 0''.12$ —around a pixel (pixel scale $= 0''.129$). The data obtained between the reads can be treated as independent 25 s exposures that can be drizzled to restore the full resolution of WFC3. In Momcheva et al. (2017) and Mowla et al. (2019b) we demonstrated that the resolution of the WFC3 camera is preserved in this process, and the measured structural parameters of the galaxies are consistent with those measured in guided observations (Cutler et al. 2022).

2.2. Observations

The DASH method was used in the Cycle 23 and 28 3D-DASH programs (Program ID: GO-14114 and GO-16259) to obtain 1256 WFC3 H_{160} pointings in 157 orbits, covering an area of 1.35 deg^2 in the COSMOS field. The design of the mosaic was constrained by the available orientations. To ease scheduling no initial ORIENT constraints were imposed. After scheduling windows were assigned, the final mosaic was designed, constrained by the ORIENTs that were allowed within each of the windows. A consequence of this strategy is that the final mosaic has gaps, as the wide range of orientations precluded the design of a fully contiguous mosaic that also avoids severe overlaps between pointings. The Cycle 23 data were obtained between 2016 November and 2017 June, while the Cycle 28 data were obtained between 2020 December and 2022 March.

Each orbit consists of a guide star acquisition, followed by a single guided exposure. Next, the stream of corrections from the fine guidance sensor is turned off, and the telescope is moved to the second exposure. Guiding remains off for the next six exposures. The exposure times, and hence the number of independent reads within each exposure, were determined by the requirement to fit eight pointings in a single orbit.

Following the 2018 failure of one of the HST gyros, a new, previously dormant gyro was turned on. The new gyro exhibited extremely high bias at the start of operations, which

¹⁸ HST is limited to two acquisitions per orbit by policy, see [STIS Instrument Handbook](#).

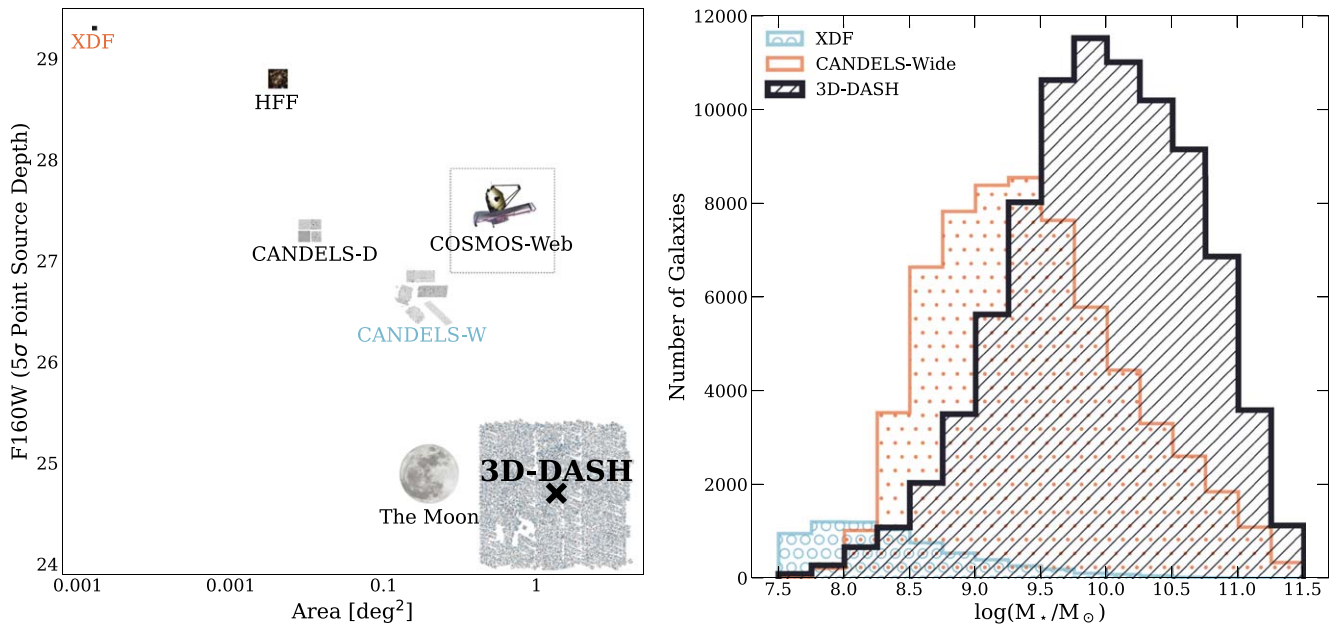


Figure 1. Left: area vs. depth for WFC3/F160W imaging surveys. The area of the thumbnails is proportional to the area of the surveys, which includes the Hubble Extreme Deep Field (XDF, 330 orbits; Illingworth et al. 2013), Hubble Frontier Fields (Lotz et al. 2017; Shipley et al. 2018), and the CANDELS (900 orbits; Koekemoer et al. 2007). The upcoming COSMOS-Web survey (Kartaltepe et al. 2021) with the James Webb Space Telescope (JWST; Gardner et al. 2006) is shown by the open box with JWST. The 3D-DASH survey, observed using the Drift And Shift technique (Momcheva et al. 2017), is shown with a black cross. It subsumes COSMOS-DASH (57 orbits observed with DASH; Mowla et al. 2019b) and other ancillary data in the COSMOS field, which are listed in Table 3. Right: the number of galaxies per stellar mass bins that are observed within three tiers of the HST extragalactic wedding cake: XDF (Iyer, Mowla in prep.; Sorba & Sawicki 2018), 3D-HST/CANDELS (Leja et al. 2020), and 3D-DASH (COSMOS2020; Weaver et al. 2022). For XDF and 3D-HST/CANDELS, we have selected all galaxies from their respective catalogs within $0.1 < z < 3$. For 3D-DASH we have selected galaxies from the COSMOS2020 catalog with $H < 23$ within $0.1 < z < 3$ (the requirement for size measurement with $\delta r_e/r_e < 0.2$ from Cutler et al. 2022). We note that these different surveys are not calibrated to match, except for the use of the same initial mass function, and thus we expect systematic uncertainties in stellar mass on the order of 0.2 dex between the samples that are not corrected here.

Table 1
Summary of the Imaging Data Released in the 3D-DASH_v1.0

3D-DASH IMAGING SUMMARY	
Position (J2000)	R.A. $10^{\text{h}}00^{\text{m}}25^{\text{s}}.4$, Decl. $+02^{\circ}12'21''.0$
DASH-only area	1.35 deg ²
Ancillary area	0.21 deg ²
Area (combined)	1.43 deg ²
Instrument/Filter	WFC3/F160W
Exposure Dates (DASH)	2016 November–2017 June (Cycle 23) 2020 December–2022 March (Cycle 28)
Exposure Dates (Ancillary)	2010–2022
Number of DASH pointings	1256
Zero-point H_{160}	25.95
Pixel scale	0''.1
Median DASH-only depth ^a	24.72 ± 0.17
Median ancillary depth ^a	26.88 ± 0.40
Median 3D-DASH depth ^a (including ancillary)	24.74 ± 0.20
DOI	doi:10.17909/srcz-2b67
Archive Link	https://archive.stsci.edu/hlsp/3d-dash

Note.

^a 5σ H_{160} point-source depth.

necessitated certain changes in the observatory controls which led to differences between the GO-14114 (executed prior to the gyro switch) and GO-16259 (executed post-switch) observations. The orbital visibility in COSMOS post-switch is shorter by 290 s, the duration of guide star acquisitions and commanded offsets is increased and the observatory is not allowed to execute an offset during the 5 minutes after the guide star acquisition. The combined effect is a shorter length of the science exposure.

With the additional constraints of the SPARS25 sampling sequence (exposure times must change by integer factors of 25 s) and avoiding buffer dump interruptions, we find a new optimum sequence of exposure times. The total exposure time in the orbit is 350 s shorter than in GO-14114 (1774 versus 2124 s). Figure 5 and Table 2 show the APT graphical representation of a single GO-16259 orbit and the sequence of events, respectively. These can be compared to Figure 2 and Table 1 in Momcheva et al. (2017).

The 3D-DASH WFC3/F160W imaging will be supplemented by WFC3/G141 grism spectroscopy, executed in Cycles 28 and 29 in 159 orbits (see Figure 4 for the grism observation footprint). 3D-DASH will increase the area observed with infrared grism spectroscopy by almost an order of magnitude and map the spatially resolved emission lines of over a thousand star-forming galaxies at cosmic noon, providing crucial information on the buildup of disks and bulges of galaxies. Similar to the imaging, the grism spectroscopy will cover the ACS COSMOS field, observed efficiently in 1272 pointings using the DASH technique.

3. The 3D-DASH Imaging Mosaic

3.1. Preparation of 3D-DASH Mosaic

Owing to the shifts during the exposures, the reduction of DASH data is more complex than that of guided exposures. Here we provide a summary of the reduction procedures; we also refer to Momcheva et al. (2017) where the reduction of a subset of the 3D-DASH¹⁹ data were first described.

¹⁹ We refer to the full combined data set as 3D-DASH, subsuming the pilot COSMOS-DASH data set.

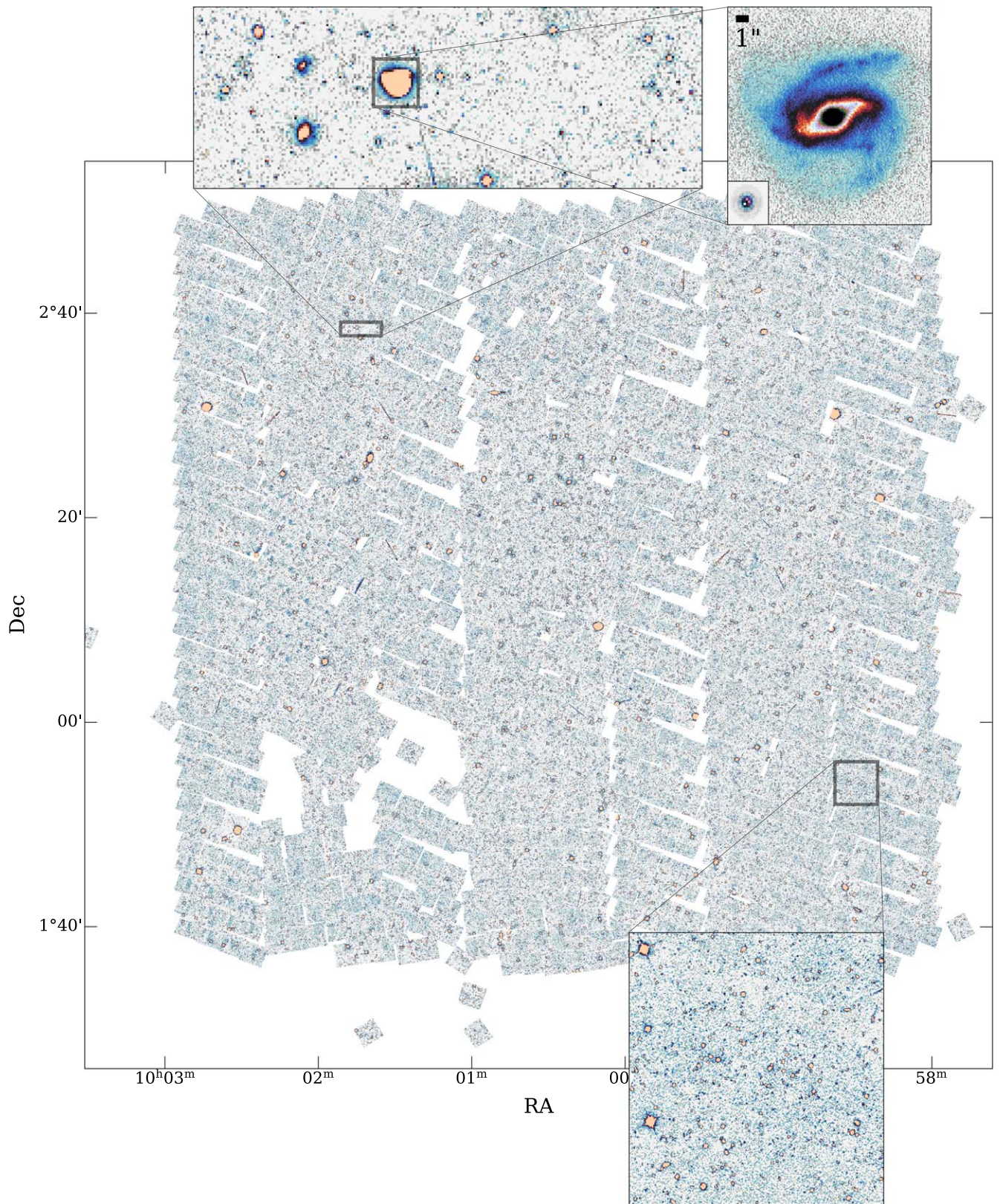


Figure 2. The 3D-DASH F160W mosaic. The area contributed by 3D-DASH is 1.35 deg^2 ; the total area with all ancillary F160W data in the COSMOS field, including the deeper CANDELS imaging and various other archival data sets listed in Table 3, is 1.43 deg^2 . The zoomed-in panels reveal the wealth of bright objects that can be studied in this high-resolution shallow tier of the extragalactic wedding cake. The point-spread function at the location of the zoomed-in galaxy is shown in the inset.

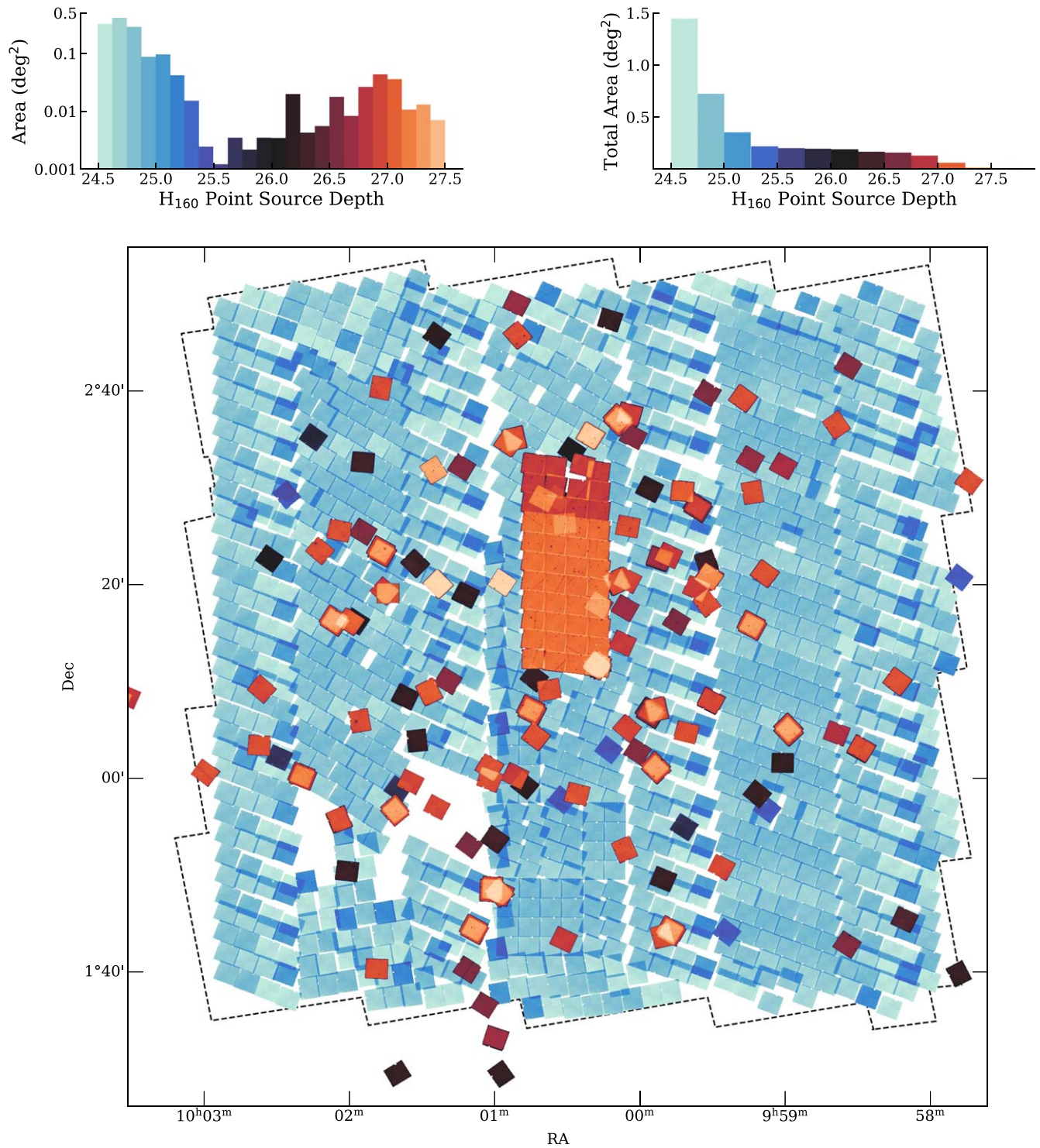


Figure 3. Bottom: the 3D-DASH H_{160} point-source depth map. The area contributed by 3D-DASH is 1.35 deg^2 shown by the blue pointings. The total area is 1.43 deg^2 and includes all ancillary data in the COSMOS field shown by black to orange pointings, including the deeper CANDELS imaging and various other archival data sets listed in Table 3. The dashed-black outline shows the 1.64 deg^2 covered by ACS/F814W (Koekemoer et al. 2007). Top left: distribution of point-source depths in 3D-DASH mosaic, with the wider and shallower images coming from the DASH programs in Cycles 23 and 28, and the deeper images coming from CANDELS and other ancillary programs. Top right: the cumulative area available in 3D-DASH below a certain point source depth.

Each DASH orbit consists of one guided and seven unguided exposures with offsets of roughly $2'$ between each. Momcheva et al. (2017) describe the overall mosaic strategy and detailed commanding instructions for the DASH visits. For uniformity of the data reduction, we process both guided and unguided exposures using the same analysis pipeline as outlined below.

The raw WFC3/IR images were downloaded from the Mikulski Archive for Space Telescopes (MAST)²⁰ and processed into calibrated exposure ramps (“IMA” products) with the `calwf3` pipeline after disabling the pipeline cosmic

²⁰ <http://archive.stsci.edu>

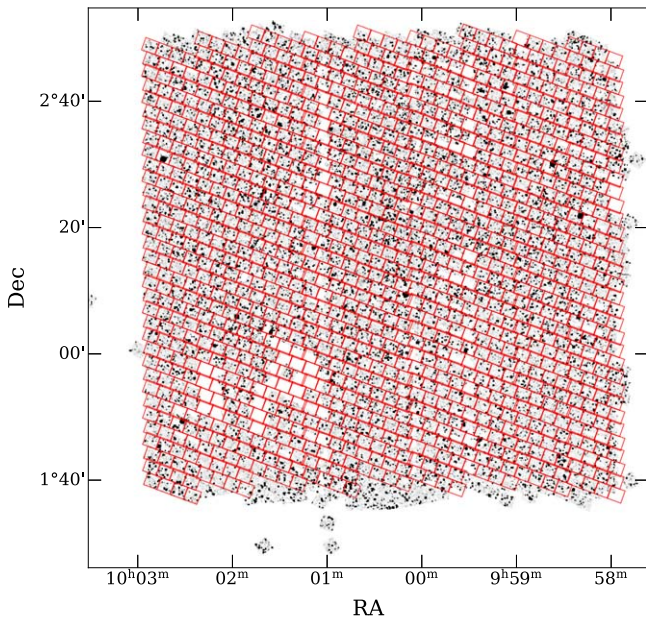


Figure 4. The 3D-DASH WFC3/G141 grism spectroscopy footprint covering the COSMOS field. In Cycles 28 and 29, grism observations of 1.43 deg² area will be obtained in 1272 pointings in 157 HST orbits using the Drift And Shift technique.

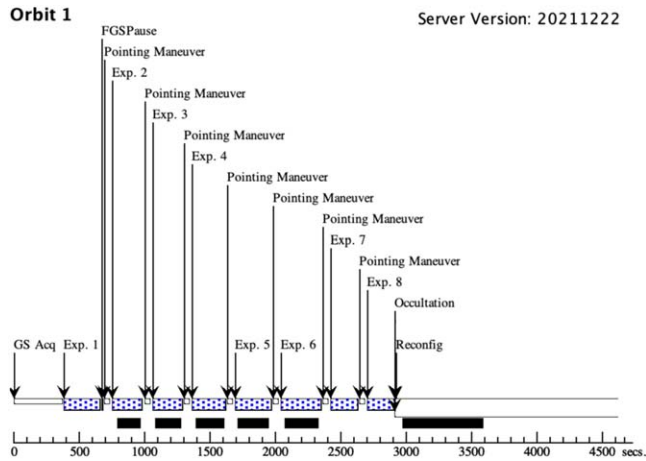


Figure 5. Graphical representation of a single Drift And Shift orbit (Visit 1 of GO-16259). Only the first pointing is guided (PCS Mode = FINE). Blue, dotted bars indicate science exposures. Black bars are buffer dumps. The total exposure time is 1774 s, corresponding to 56% of the total orbital visibility.

ray identification step (CRCORR=False). The IMA files provide a measure of the total charge on the detector sampled every 25 s over the duration of the exposure (253 or 278 s for exposures with NSAMP = 12 and 13, respectively). To reduce the degradation of the image quality of a given exposure due to the telescope drifts, we take image differences up the ramp and generate NSAMP - 2 essentially independent calibrated exposures with drifts now integrated over 25 s rather than the full exposure duration.²¹ The properties of these difference images are essentially identical to normal calibrated WFC3/IR “FLT” products, though with slightly different noise characteristics. Taking image differences increases the effective read noise by a factor of $\sqrt{2}$ and the read noise of two adjacent image

differences will be anticorrelated as the measured (noisy) flux of a given read appears as negative in the first difference image and positive in the second. In the case of guided exposures with no drifts, the image differences are equivalent to taking the pixel values of the last read minus the first, with read noise from just those two reads. The differences do not cancel out for sequences with drifts, where the pixel indices of the difference images are effectively shifted when they are combined into the output mosaic.

The DASH observations produce $N \times 7 \times (\text{NSAMP} - 2)$ difference image “exposures,” with N the number of orbits. These exposures are processed in an identical way to the N -guided exposures that are taken at the start of each orbit, and with all guided archival observations in the COSMOS field. We first compute an internal alignment of the visit exposures using sources detected in the images (both stars and galaxies), which corrects the DASH drifts between samples and small pointing errors typical of the guided sequences. We generate a small mosaic of the visit exposures to detect fainter sources and align these mosaics to galaxies in the F814W catalogs provided by the COSMOS collaboration (Koekemoer et al. 2007). Point sources are excluded from the catalog alignment as stars can have significant proper motions between the ACS COSMOS and DASH epochs. Since we do not identify cosmic rays in the DASH exposures at the pipeline level as with normal WFC3/IR exposures, we detect and mask the cosmic rays using the standard tools of the AstroDrizzle (Gonzaga 2012) package when creating the combined visit/pointing image (turning on cosmic ray identification is useful even for the guided exposures to mask unflagged hot pixels and weaker cosmic rays missed by calwf3). In the pilot COSMOS-DASH program, several sequences of eight pointings were broken up due to South Atlantic Anomaly (SAA) passages. There was typically a large offset of 10”–15” between the “before” and “after” exposures, due to the spacecraft drift during the SAA passage; nevertheless, no observable degradation of the PSF was found in these sequences. However, the interruption of DASH orbits by SAA passages lowered the efficiency of the observatory because the orbit following the SAA passage was only 1/4 full. For this reason the planning team recommended that we avoid SAA passages and schedule all eight pointings within a single orbit.

The requirement of three functioning HST gyros is crucial for the optimum execution of the DASH technique. In recent years, multiple gyro failures have made DASH observations challenging. Here we show that the average drift between reads has increased from 0”02 in the pilot COSMOS-DASH survey in 2017 to 0”15 in 2021 and is over 0”5 per read for ~5% of pointings as shown in Figure 7. The exact cause of this increase is not clear. This increased drift has resulted in a more irregular overlapping of pointings and some noticeable gaps in the mosaic, as can be seen in Figure 3. It has also resulted in increased background noise and thus a lower point-source depth than the pilot COSMOS-DASH program (see Section 3.4).

The full set of ~5000 aligned DASH exposures, together with all other existing H_{160} data in the COSMOS field, are then drizzled into a single, large mosaic using Astrodrizzle. The weight map scales with both the variations in exposure time and the impact of drifting across the final mosaic, where lower weight corresponds to higher drift and/or shorter exposure times. Both the science image and weight maps are drizzled to a pixel scale of 0”1 using a square kernel and with

²¹ Software to split DASH exposures into difference images is provided at <https://github.com/gbrammer/wfc3dash>.

Table 2
Structure of a Single GO-16259 Orbit

Step	Event	Changes to Keywords	Duration	Exposure Time
1	guide star acquisition	...	383 s	
2	guided exposure, position 1	PCS Mode=FINE SAMP=SEQ=SPARS50 NSAMP=6	295 s	253 s
3	stop FGS corrections	...	21 s	
4	offset to position 2	...	59 s	
5	unguided exposure, position 2	PCS Mode=GYRO SAMP=SEQ=SPARS25 NSAMP=9	245 s	203 s
6	offset to position 3	...	59 s	
7	unguided exposure, position 3	NSAMP=9	245 s	203 s
8	offset to position 4	...	59 s	
9	unguided exposure, position 4	NSAMP=10	270 s	228 s
10	offset to position 5	...	58 s	
11	unguided exposure, position 5	NSAMP=11	295 s	253 s
12	offset to position 6	...	59 s	
13	unguided exposure, position 6	NSAMP=12	320 s	278 s
14	offset to position 7	...	59 s	
15	unguided exposure, position 7	NSAMP=8	220 s	178 s
16	offset to position 8	...	58 s	
17	unguided exposure, position 8	NSAMP=8	220 s	178 s
	Unused orbital visibility:		0 s	
	Total duration and exposure time:		2925 s	1774 s

$\text{pixfrac} = 0.8$. The final mosaic of the 3D-DASH image is 53248×53248 pixels and is centered at RA = 10:00:28.6, DEC = +02:12:21.0. The image is shown in Figure 2 and the point-source depth map created from the weight map (using the average noise in $0''.3$ diameter apertures, details in Section 3.3) is shown in Figure 3. All our data products are available at MAST as a ²²High Level Science Product and ²³here. The science images and their corresponding weight maps are available in three formats:

1. Full 3D-DASH mosaic²⁴
2. 3D-DASH mosaic (see footnote 22) divided into 256 (16×16) tiles
3. Full DASH-only mosaic.

3.2. Point-spread Function of 3D-DASH

We created a grid of point-spread functions (PSF) for the 3D-DASH mosaic using Grizli²⁵ to shift and drizzle HST empirical PSFs (Anderson et al. 2015) at the positions of 12335 stars brighter than $I < 25$ from the Hyper Suprime-Cam Subaru Strategic Program (Aihara et al. 2021). Some example position-dependent empirical PSFs and the stars at their positions are shown in Figure 6. These 12,335 stars sample the entire 3D-DASH mosaic area (see right panel of Figure 7), including the CANDELS region. We also provide a PSF generator tool²⁶ to determine the PSF at any location within the 3D-DASH footprint.

While the position angle of each pointing is largely aligned, there are subtle variations visible in Figure 3 that motivate our

decision to adopt a position-dependent PSF. When comparing the orientation of star spikes across the mosaic in Figure 5(b), we further see several cases where multiple orientation angles are coadded. The curves of growth, which show the fraction of light enclosed as a function of aperture size, for the DASH H_{160} PSFs, normalized at $2''$, are shown in the left panel of Figure 6 for both the synthetic PSF and the empirical PSF from the stars. The PSFs are in agreement with each other and with the encircled energy as a function of aperture provided in the WFC3 handbook when also normalized to a maximum radius of $2''$. This demonstrates that the DASH technique does not introduce significant smoothing.

To check the effect of the drift on the shape of the point-spread functions, we measured the axis ratios in the 12335 stars using GALFIT (Peng et al. 2010). While most of the stars have axis ratios >0.8 , we notice that stars in certain regions demonstrate flattening see 7. These regions coincide with regions of higher drift, which affected some orbits of Cycle 28. The regions of high drift ($>0''.5$ per pointing) account for 5.4% of the entire 3D-DASH area. This is reflected in the shape of the PSFs, with 4.3% of PSFs having an axis ratio <0.5 .

3.3. Background Noise

The depth of the mosaic is determined by the background noise, which is expected to scale with the size of the aperture that is used for photometry. To determine how the background noise scales with aperture size, we measure the distribution of counts in empty regions of increasing size within the noise-equalized F160W image. For each aperture size, we measure the flux in 10,000 apertures placed at random positions across the combined 3D-DASH mosaic with both the DASH and the “standard” depth pointings. DASH depths are selected with a weight <100 , and “standard” depths have a weight >100 . Apertures that overlap with sources in the detection segmentation map are randomly moved until they no longer overlap with a source. Figure 8 shows

²² <https://doi.org/10.17909/srcz-2b67>

²³ <https://archive.stsci.edu/hlsp/3d-dash/>

²⁴ Combined DASH pointings and ancillary data.

²⁵ <https://grizli.readthedocs.io>

²⁶ <https://tinyurl.com/3ddashpsfgenerator>

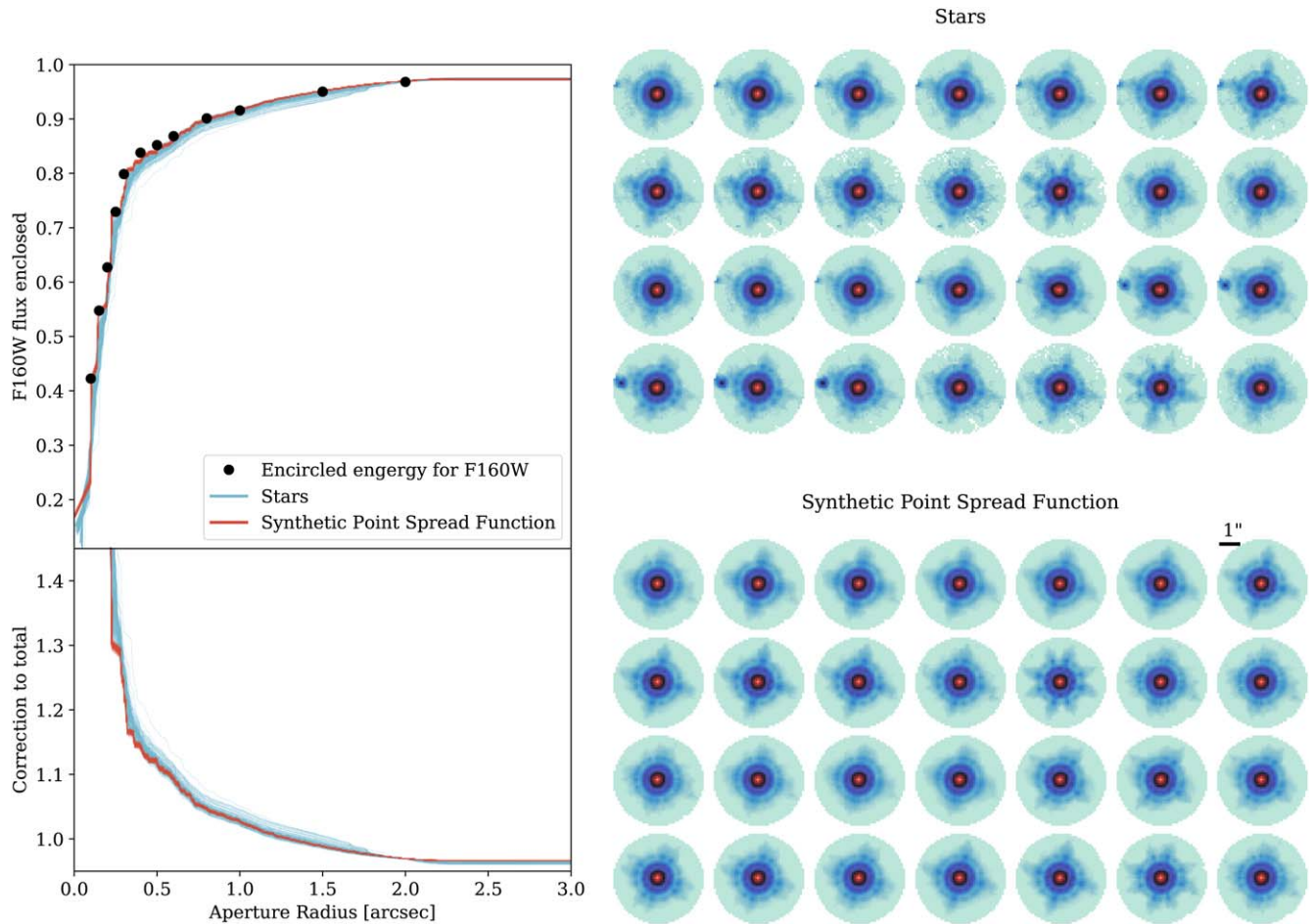


Figure 6. The point-spread function (PSF) and growth curve of 3D-DASH. Right: example point-spread functions from the 3D-DASH field. The top panel shows the stars selected from the Hyper Suprime-Cam Subaru Strategic Program (Aihara et al. 2021) while the bottom panel shows synthetic position-based point-spread functions. Left: H_{160} growth curve. The upper panel shows the fraction of total light enclosed as a function of radius from all the used H_{160} PSF stamps. This is calculated as the fraction of light inside a given radius to the light inside $2''$, $f(r)/f(2'')$, renormalized to the fraction of total light enclosed within $2''$ (97% from WFC3 Instrument Handbook). (The blue lines show the growth curve of stars while the red lines are of the synthetic PSFs. The PSFs of the entire field are consistent with each other as shown by the blue and red lines. The black points show the encircled energy as a function of aperture size, also normalized to $2''$, from the WFC3 Instrument Handbook. The lower panel shows the correction to total flux for point sources across the mosaic with a circularized Kron radius equal to the aperture radius on the x -axis. This is the inverse of the growth curves shown in the upper panel ($f(2'')/f(r)$). The minimum Kron radius is set to $0.3''$, which requires a maximum correction of 1.4.

the distribution of flux counts for increasing aperture size ranging from 0.2 to $2''$ diameters in the 3D-DASH image. Each histogram can be well described by a Gaussian, with the width increasing as aperture size increases. The increase in standard deviation with linear aperture size $N = \sqrt{A}$, where A is the area within the aperture, can be described as a power law. A power-law index of 1 would indicate that the noise is uncorrelated, whereas if the pixels within the aperture were perfectly correlated, the background noise would scale as N^2 . The right-hand panel of Figure 8 shows the measured standard deviation as a function of aperture size in the noise-equalized 3D-DASH image. We fit a power law of the form

$$\sigma = \sigma_1 \alpha N^\beta, \quad (1)$$

where σ_1 is the standard deviation of the background pixels fixed to a value of 1.5 here, α is the normalization and $1 < \beta < 2$ (Whitaker et al. 2012b). The fitted parameters are shown in Figure 8. The power-law fit is shown by the solid line in the figure.

We also separate individual DASH apertures based on the program they were taken in (Cycle 23 COSMOS-DASH or Cycle 28 3D-DASH) to determine if the more recent DASH

observations differ significantly in noise properties from the pilot program. On average, the 3D-DASH data with low drift rates similar to the pilot COSMOS-DASH data are deeper with a slightly steeper power-law index that supports more correlated noise (see Figure 8). Those pointings with the highest drift instead have shallower depths (noisier data) and $\beta \sim 1$, suggesting uncorrelated noise. This makes sense as the drift rate in these cases is larger than the PSF itself between reads.

3.4. Point-source Depth

With the PSF and noise in hand we can calculate the photometric depth of the mosaic. In the right panel of Figure 8 we show the 5σ depth as a function of aperture size. Apertures of a given size are placed at random positions within the mosaic, and we then calculate the 1σ variation in the measured fluxes within these apertures. A multiplicative aperture correction is applied based on the flux that falls outside that aperture for a point source and multiplied by 5 to estimate the 5σ depth (see Skelton et al. 2014). For very small apertures the

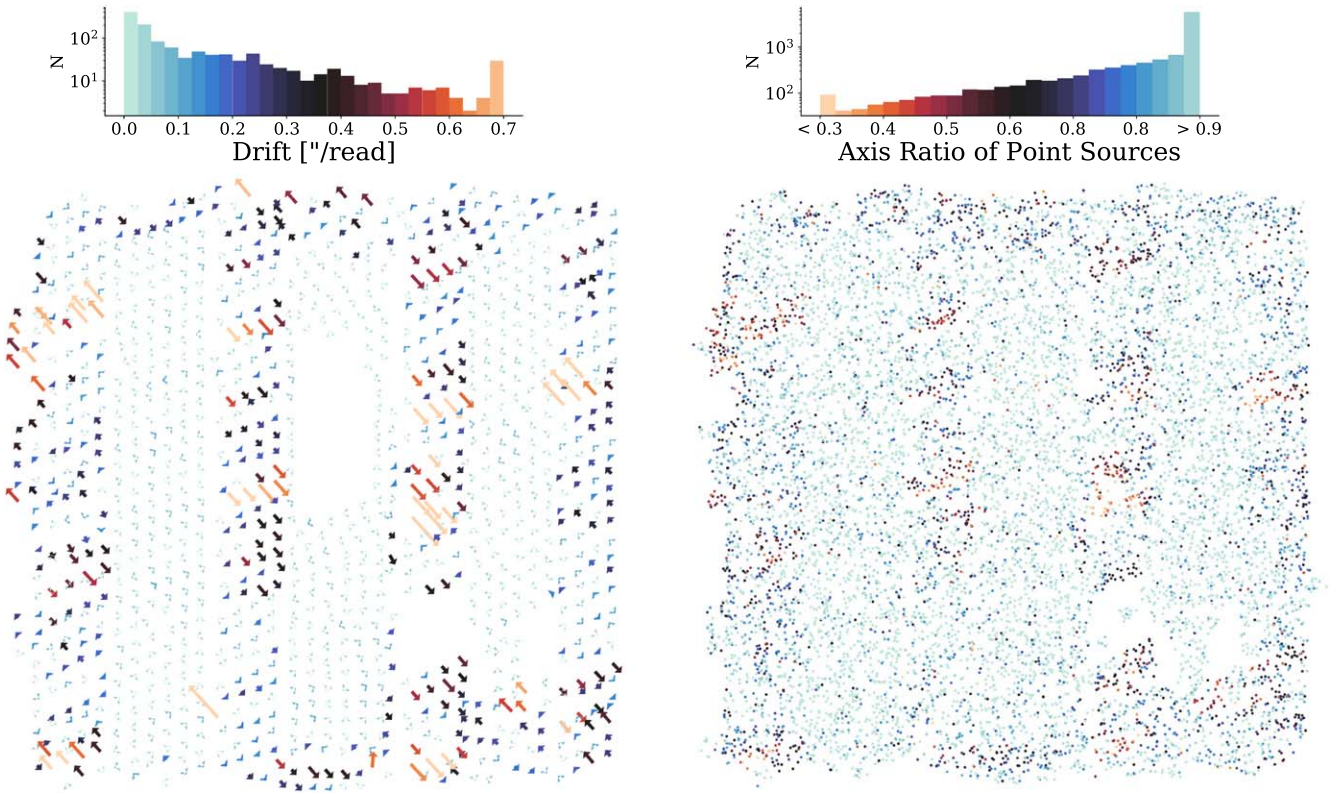


Figure 7. Left: the total drift of the telescope during an unguided exposure, with the length of the arrow representing the drift in one pointing and the color representing the average drift per read. The histogram on top shows the distribution of drifts in 3D-DASH. Right: the axis ratio of point sources in the 3D-DASH image. The point sources were identified from the Hyper Suprime-Cam Subaru Strategic Program (Aihara et al. 2021) and their axis ratios are measured using GALFIT. The point sources in the final image are elongated in regions of higher drift.

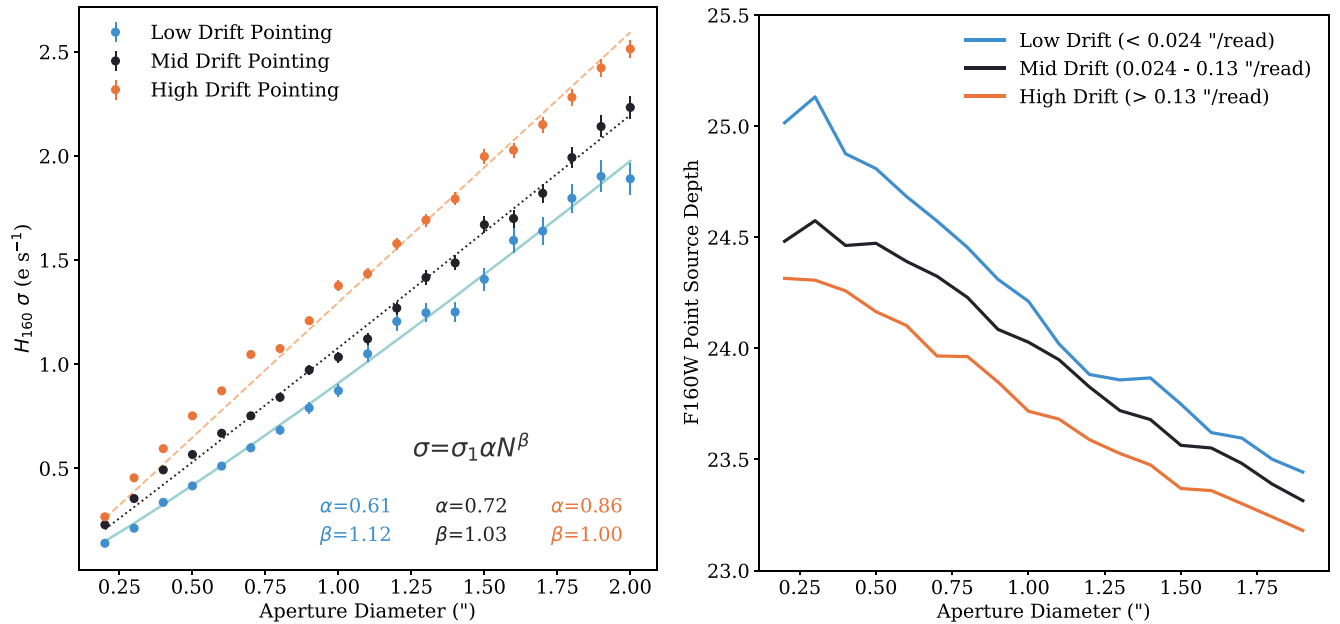


Figure 8. The background noise level and the point-source depth of 3D-DASH. To demonstrate the effect of the increased gyro drift in HST in Cycle 28, we split up our DASH-only pointings into three bins based on their drift rates: $dr < 0''.024$ (low drift), $0''.024 < dr < 0''.13$ (medium drift), and $dr > 0''.13$ per read (high drift). Left: empty aperture photometry on the mosaic to determine the background noise level. The plot shows the standard deviation of the distribution of total flux in different aperture sizes measured from the noise-equalized mosaic. The lines are power-law fits to the data, with the fit parameters shown below. The pointings with lower drifts demonstrate slightly steeper power-law index that supports more correlated noise. Right: the point-source depth is measured in different aperture diameters. The low drift pointings reach a depth similar to that of the pilot COSMOS-DASH, while high drift pointings result in shallower images.

S/N is suppressed because of the large aperture corrections that need to be applied, and for very large apertures the S/N is suppressed because of the high noise within the aperture (see,

e.g., Figure 7 in Whitaker et al. 2011). The optimal aperture for HST NIR imaging is $0''.3$, and the 5σ depth within that aperture is 24.72 ± 0.17 for 3D-DASH pointings (depth at $0''.7$ is

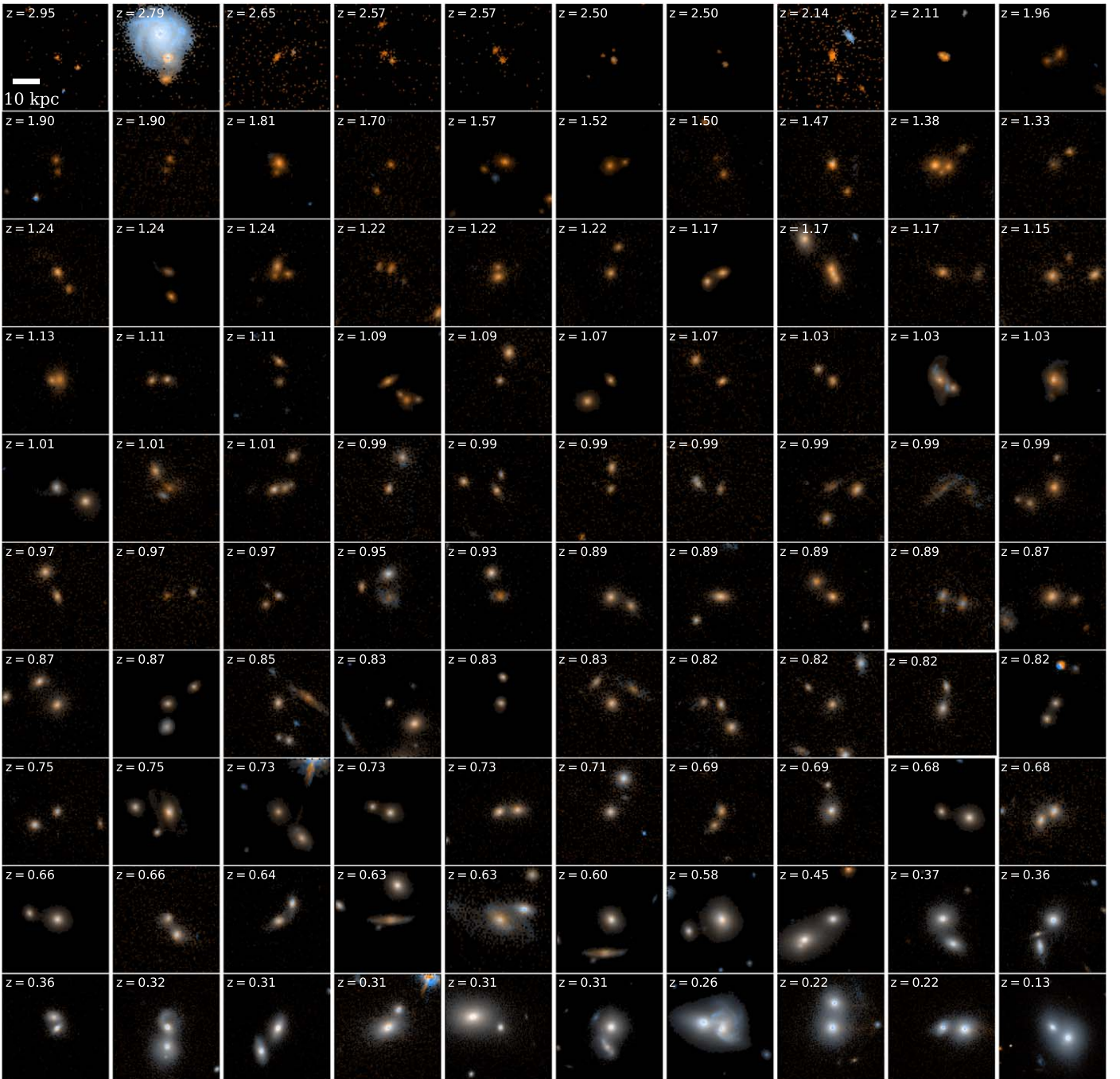


Figure 9. With the wide-area high-resolution imaging, we now have a census of rare close pair of galaxies, critical for studying the evolution of galaxy merger rates. Stamps show close pair galaxies in the 3D-DASH field with $\log(M_*/M_\odot) > 10.5$ at $z < 3.0$ with $H < 22$ and separation less than 20 kpc (2D separation with an additional cut of $z_{\text{diff}} < 0.05$) from the UVISTA catalog. The galaxies are sorted by their redshift, which is shown in the top left corner. Each stamp is 40 kpc \times 40 kpc and is created using DASH-area only WFC3/F160W and ACS/F814W images.

24.4 ± 0.2). This can be compared to the expected depth for guided exposures of the same exposure time, as determined by the Exposure Time Calculator. The expected depth is ≈ 25.2 , which means that the use of the DASH technique imposes a penalty of $\approx 36\%$ on the image depth due to increased gyro drift.

The Cycle 28 3D-DASH has an average point-source depth ~ 0.4 shallower than COSMOS-DASH. The cause of this increased noise and shallower imaging is likely increased drift rates in the DASH observations due to the new gyros. To check for this, we split the new DASH pointings into three equal-sized bins based on

drift rates: $dr < 0''.024$ (low drift), $0''.024 < dr < 0''.13$ (medium drift), and $dr > 0''.13$ per read (high drift) (see Figure 8). The pointings with low drift rates reach a point-source depth ($H_{160} \sim 25.1$) similar to that of COSMOS-DASH, while the pointings with high drift rates produce shallower images ($H_{160} \sim 24.3$).

4. Example Images and Science Cases

The purpose of the present paper is to describe the 3D-DASH program and its first major data product, a WFC3/IR

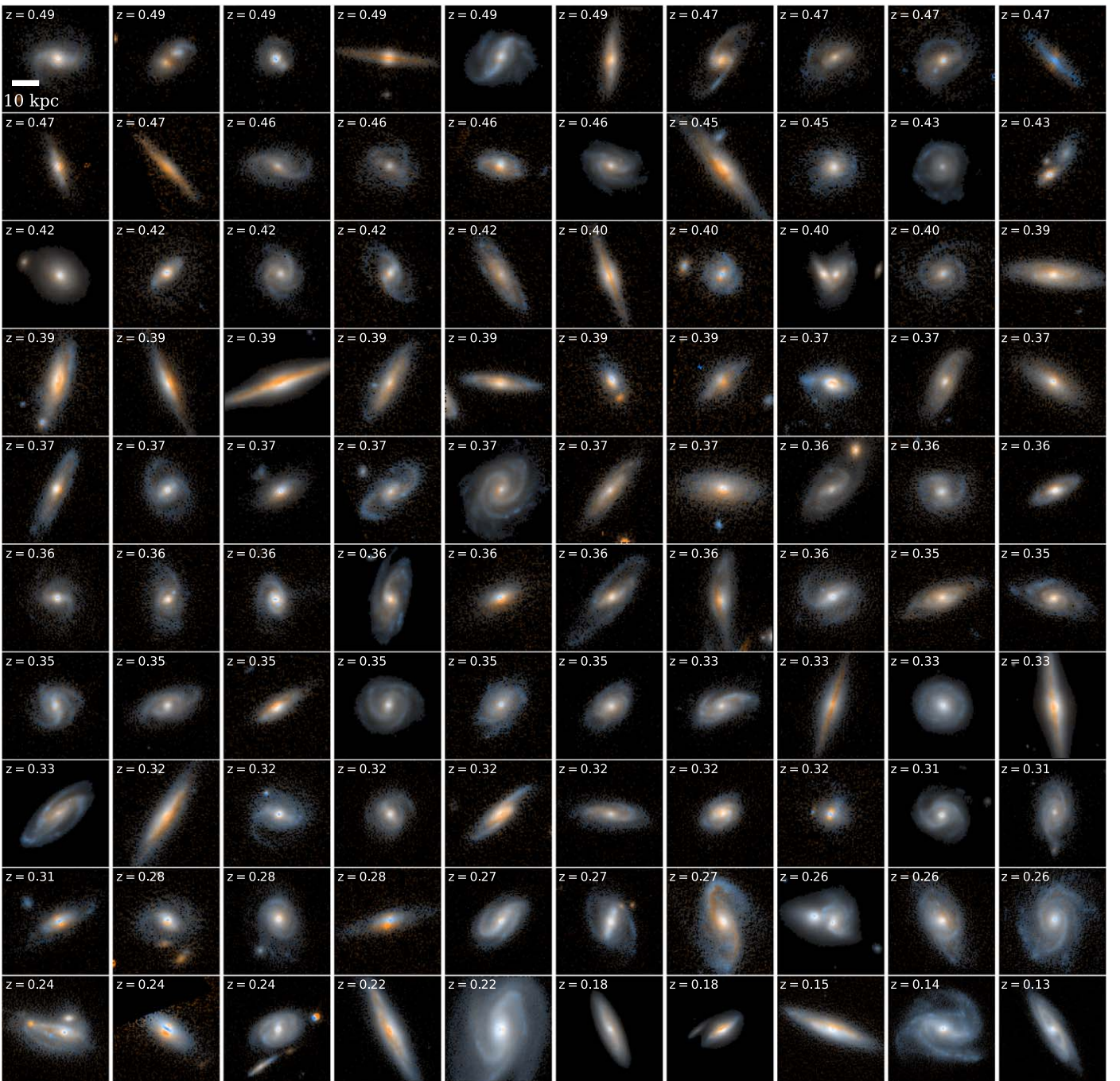


Figure 10. The wide-area imaging combined with grism spectroscopy gives a census of the morphology of star-forming regions of the rare massive star-forming galaxies in the last 5 Gyrs. The stamps show the most massive star-forming galaxies (selected with $U - V$ and $V - J$ color cuts from Whitaker et al. 2011) in the 3D-DASH field with $\log(M_*/M_\odot) > 10.8$ at $z < 0.5$ from the UVISTA catalog. The galaxies are sorted by their redshift, which is shown in the top left corner. Each stamp is $40 \text{ kpc} \times 40 \text{ kpc}$ and is created using DASH-area only WFC3/F160W and ACS/F814W images.

H_{160} mosaic of the COSMOS field. Besides the 3D-DASH data themselves, we include data from 18 previous imaging programs in the mosaic, including the Cycle 23 COSMOS-DASH pilot program. These data are not deep by conventional HST standards: the exposure time at most positions in the mosaic is only ≈ 250 s. Nevertheless, thanks to HST’s superb resolution and the low background from space, the resulting 5σ point-source depth of 24.72 ± 0.17 ($0''.3$ diameter aperture) and 24.4 ± 0.2 ($0''.7$ diameter aperture) adds a high-resolution shallow tier to the deep observations from the ground (e.g., NEWFIRM Median Band Survey, Whitaker et al. 2011;

UVISTA, Muzzin et al. 2013; Hyper Suprime-Cam Subaru Strategic Program, Aihara et al. 2021).

The data have a wide range of science applications, and are particularly powerful for studies that are currently not limited by depth but by resolution in the NIR. In Figures 9, 10 and 11, we show example galaxy images for three such projects.

4.1. Massive Close Pairs

In Figure 9 we show massive close pairs, many of which are expected to be mergers in progress that lead to the buildup of

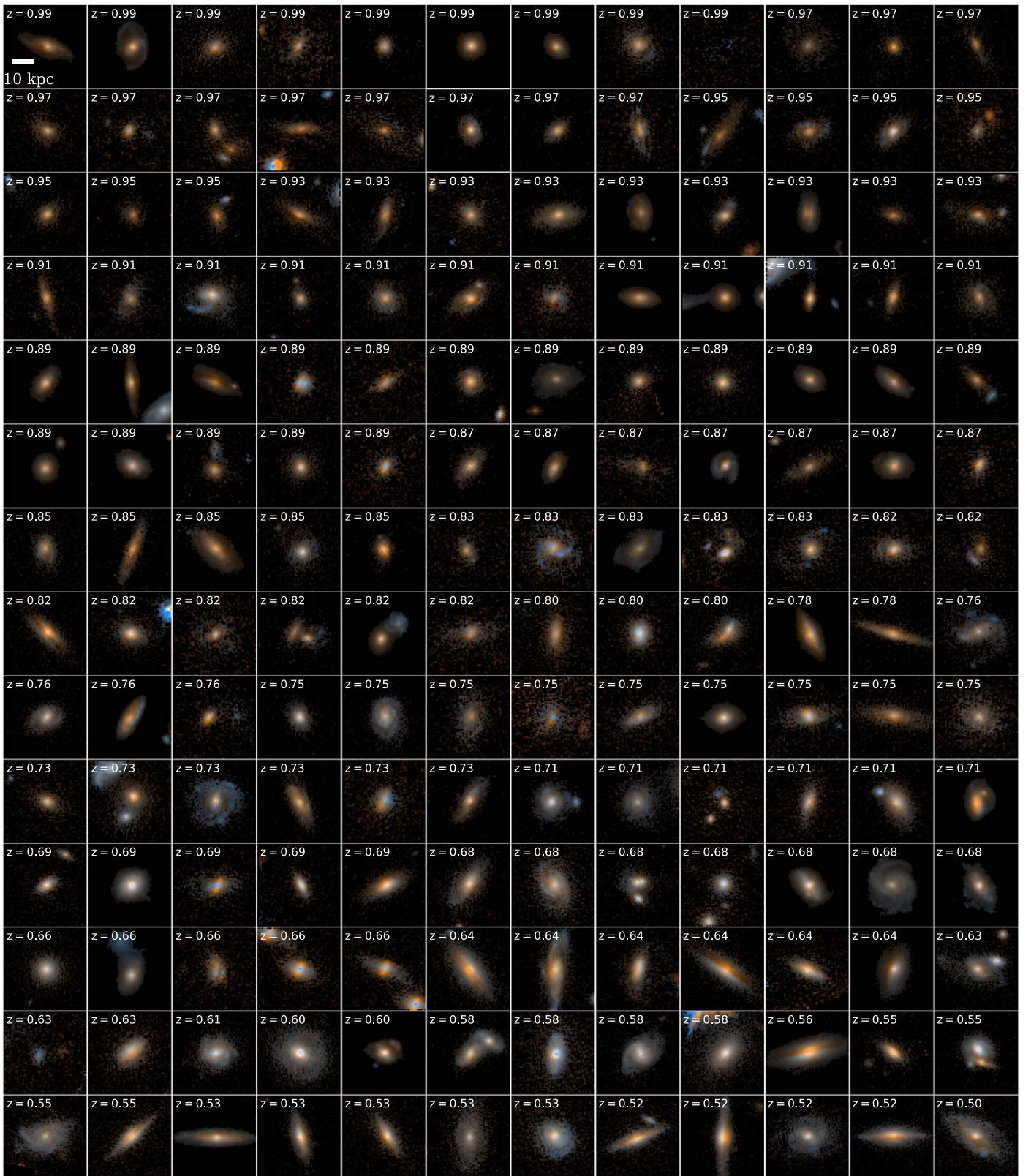


Figure 11. The wide-area imaging combined with HST grism spectroscopy, deep ground-based multiwavelength imaging (UVISTA Muzzin et al. 2013), and spectroscopy (LEGA-C van der Wel et al. 2016), gives a census of the evolution of star-forming regions of the rare massive star-forming galaxies at $0.5 < z < 1.0$. The stamps show the most massive star-forming galaxies (selected with $U - V$ and $V - J$ color cuts from Whitaker et al. 2011) in the 3D-DASH field with $\log(M_*/M_\odot) > 11$ at $0.5 < z < 1.0$ from the UVISTA catalog. The galaxies are sorted by their redshift, which is shown in the top left corner. Each stamp is $40 \text{ kpc} \times 40 \text{ kpc}$ and is created using DASH-area only WFC3/F160W and ACS/F814W images.

Table 3
Data Included in the Final H_{160W} 3D-DASH_v1.0 Mosaic

Program Number	HST Cycle	Number of Pointings	Program Name	Principal Investigator
12167	18	28	Resolving the Matter of Massive Quiescent Galaxies at $z = 1.5 - 2$	Marijn Franx
12440	19	176	Cosmic Assembly NIR Deep Extragalactic Legacy Survey—GOODS-South Field, Non-SNe-Searched Visits	Sandra Faber, Henry Ferguson
12461	19	23	Supernova Follow-up for MCT	Adam Reiss
12578	19	14	Constraints on the Mass Assembly and Early Evolution of $z \sim 2$ Galaxies: Witnessing the Growth of Bulges and Disks	Natascha Förster Schreiber
12990	20	52	Size Growth at the Top: WFC3 Imaging of Ultra-Massive Galaxies at $1.5 < z < 3$	Adam Muzzin
13294	21	6	Characterizing the formation of the primordial red sequence	Alexander Karim
13384	21	4	A Simultaneous Measurement of the Cold Gas, Star Formation Rate, and Stellar Mass Histories of the Universe	Dominik Riechers
13641	22	36	A Detailed Dynamical And Morphological Study Of $5 < z < 6$ Star, Dust, and Galaxy Formation With ALMA And HST	Peter Capak
13657	22	116	Probing the Most Luminous Galaxies in the Universe at the Peak of Galaxy Assembly	Jeyhan Kartaltepe
13868	22	44	Are Compton-Thick AGN the Missing Link Between Mergers and black hole Growth?	Dale Kocevski
14114	23	456	A Wide-Field WFC3 Imaging Survey in the COSMOS Field	Pieter van Dokkum
14721	24	40	The Fundamental Plane of Ultra-Massive Galaxies at $z \sim 2$	Christopher Conselice
14750	24	8	Exploring environmental effects on galaxy formation with WFC3 in the most distant cluster at $z = 2.506$	Tao Wang
14895	24	20	Confirmation of ultra-luminous $z \sim 9$ galaxies	Rychard Bouwens
15229	25	32	Spectroscopic redshifts and age dating of a first statistical sample of passive galaxies at $z \sim 3$	Emanuele Daddi
15692	26	24	HST imaging for an immediate study of the ISM in $z=4.5$ galaxies	Andreas Faisst
15910	27	25	Galaxy evolution in a massive $z = 2.91$ halo fed by cold accretion	Emanuele Daddi
16081	27	8	Let's Point Hubble at a Bubble!	James Rhoads
16259	28	800	3D-DASH: A Wide Field WFC3/IR Survey of COSMOS	Ivelina Momcheva

today’s giant elliptical galaxies (see, e.g., De Lucia & Blaizot 2007; Bezanson et al. 2009; Naab et al. 2009; Cooke et al. 2019). For this example, we show 3D-DASH images of galaxies selected from the ground-based UVISTA catalog of Muzzin et al. (2013) that satisfy the following conditions: $\log(M_*/M_\odot) > 10.5$ at $z < 3.0$ with $H < 22$ and separation less than 20 kpc (2D separation with an additional cut of $z_{\text{diff}} < 0.05$).

These galaxies are just-resolved in ground-based data, but it is not possible to measure the properties of the individual objects. In the 3D-DASH data set they are clearly distinct, showing a variety of colors and morphologies. The minimum separation of close pairs in the UVISTA is set by the ground-based resolution, and Marsan et al. (2019) find that up to 1/3 of the most massive single ground-selected massive galaxies are in fact close pairs at HST resolution. This is mitigated by the 3D-DASH images, which provide a resolution high enough to deblend the close pairs at low redshifts. This has significant implications for the high-mass end of low- z ground-based mass functions, as well as the inferred evolution of galaxies from techniques such as abundance matching (e.g., Behroozi et al. 2013) or empirical methods (Moster et al. 2018; Behroozi et al. 2019). In addition, current measurements of the massive galaxy merger rate at $z \gg 1$ are still uncertain and model dependent (e.g., Duncan et al. 2019; Pena & Snyder 2021). A 3D-DASH-selected catalog will identify a complete sample of apparent massive galaxy close pairs, further constraining the contribution of mergers to the buildup of massive galaxies.

4.2. Massive Star-forming Galaxies

A second example is shown in Figure 10. These are relatively bright and large galaxies at $z < 0.5$ that are easily detected and studied from the ground. While these low redshift galaxies are spatially resolved enough from the ground for simple morphological measurements such as size and compactness, they are not resolved enough for detailed morphological analysis pertaining to their growth. The combination of H_{160} and I_{814} from 3D-DASH and ACS COSMOS provides spatially resolved morphological information at two distinct wavelengths and enables the identification of star-forming knots and dust lanes.

The increased spatial resolution also allows for the identification and analysis of clumpy star formation (Guo et al. 2018; Huertas-Company et al. 2020). The characteristics of clumps, including numbers and lifetimes, as well as morphological features like tidal tails have important implications for the strength and mechanisms of stellar feedback and galactic winds (Elmegreen et al. 2021; Dekel et al. 2022).

4.3. Cosmic Noon Counterparts of Massive Galaxies

A third example is shown in Figure 11, which are the intermediate redshift counterparts of star-forming massive galaxies shown in Figure 10. These are relatively bright and large galaxies at $0.5 < z < 1.0$ that have deep spectroscopic observations from the ground in the LEGA-C survey (van der Wel et al. 2016) but which are not spatially resolved in the deep ground-based NIR imaging (UVISTA; Muzzin et al. 2013). At $z > 0.5$ the $I-H$ colors are critical for interpreting the morphologies, as they enable the identification of dust, star-forming regions, and old stellar populations and—more generally—the conversion of light-weighted to mass-weighted images (Förster Schreiber et al. 2011; Wuyts et al. 2012; Suss

et al. 2019). These images can be combined with the myriad of spectroscopic programs in the COSMOS field (such as van der Wel et al. 2016), for a comprehensive description of the buildup of the Hubble sequence over the past 5–8 Gyr.

5. Summary and Outlook

In 2015 we demonstrated the capability of HST to observe wide area efficiently using the Drift And SHift technique. It was implemented in the COSMOS-DASH program which imaged 0.49 deg^2 of the three deep stripes of the UltraVISTA fields. 3D-DASH extends this program by adding grism spectroscopic observations and by imaging the remaining area of the ACS COSMOS field. Here, we combine the newly obtained 3D-DASH pointings with archival data in the COSMOS field to produce a 1.43 deg^2 mosaic in the H_{160} filter. This is the largest area ever imaged in the NIR at this spatial resolution, a situation that will likely not change until the launch of Euclid (Laureijs et al. 2011) and Roman (Green et al. 2012; Spergel et al. 2015).

We show that the point-source depth of the mosaic is 24.74 ± 0.20 shallower than pointed observations, and that the depth correlates with the size of the drifts between exposures. As discussed in Section 3.2, the point-spread function is only slightly degraded after shifting and adding the exposures. We provide two PSFs for each position: one that is noiseless and only includes the theoretical position dependence, and a noisier empirical one that also includes the effects of in-sample drift and imperfect alignments. We recommend that researchers use both PSFs in their analyses and include any differences in outcomes in their error budgets. All our data products are available at MAST as a ²⁷High Level Science Product and ²⁸here . We also provide a PSF generator tool²⁹ to determine the PSF at any location within the 3D-DASH footprint.

We are publicly releasing this image which can be used as a complement to other data sets in the field, such as the LEGA-C spectroscopic survey (van der Wel et al. 2016), or to serve as the primary data for studies that require high-resolution data in the NIR. We anticipate that these data will also be helpful for planning JWST observations of objects in the COSMOS field. In the future we plan to provide an H_{160} -selected catalog of objects in the mosaic as well as deliver the grism observations that are part of the 3D-DASH project.

This paper is based on observations made with the NASA/ESA HST, obtained at the Space Telescope Science Institute, which is operated by the Association of Universities for Research in Astronomy, Inc., under NASA contract NAS 5-26555. Support from NASA STScI grants HST-GO-14114, HST-GO-16259, and HST-GO-16443 is gratefully acknowledged. L.M. and K.I. gratefully acknowledge support from the Dunlap Institute for Astronomy and Astrophysics through the Dunlap Postdoctoral Fellowship. The Dunlap Institute is funded through an endowment established by the David Dunlap family and the University of Toronto S.C. and K.W. wish to acknowledge funding from the Alfred P. Sloan Foundation and HST-AR-15027. K.W. acknowledge support under NASA grant No. 80NSSC20K0416. The Cosmic Dawn

²⁷ <https://doi.org/10.17909/srcz-2b67>

²⁸ <https://archive.stsci.edu/hlsp/3d-dash/>

²⁹ <https://tinyurl.com/3ddashpsfgenerator>

Center is funded by the Danish National Research Foundation under grant No. 140.

Facility: HST(STIS).

Software: Astropy (Astropy Collaboration et al. 2013, 2018), (grizli, Brammer 2019), (Astrodriizzle, Gonzaga 2012), (GALFIT, Peng et al. 2010), (Montage, Jacob et al. 2010).

ORCID iDs

Lamiya A. Mowla  <https://orcid.org/0000-0002-8530-9765>
 Sam E. Cutler  <https://orcid.org/0000-0002-7031-2865>
 Gabriel B. Brammer  <https://orcid.org/0000-0003-2680-005X>
 Ivelina G. Momcheva  <https://orcid.org/0000-0003-1665-2073>
 Katherine E. Whitaker  <https://orcid.org/0000-0001-7160-3632>
 Pieter G. van Dokkum  <https://orcid.org/0000-0002-8282-9888>
 Rachel S. Bezanson  <https://orcid.org/0000-0001-5063-8254>
 Natascha M. Förster Schreiber  <https://orcid.org/0000-0003-4264-3381>
 Marijn Franx  <https://orcid.org/0000-0002-8871-3026>
 Kartheik G. Iyer  <https://orcid.org/0000-0001-9298-3523>
 Danilo Marchesini  <https://orcid.org/0000-0001-9002-3502>
 Adam Muzzin  <https://orcid.org/0000-0002-9330-9108>
 Erica J. Nelson  <https://orcid.org/0000-0002-7524-374X>
 Rosalind E. Skelton  <https://orcid.org/0000-0001-7393-3336>
 Gregory F. Snyder  <https://orcid.org/0000-0002-4226-304X>
 David A. Wake  <https://orcid.org/0000-0002-6047-1010>
 Stijn Wuyts  <https://orcid.org/0000-0003-3735-1931>
 Arjen van der Wel  <https://orcid.org/0000-0002-5027-0135>

References

- Aihara, H., AlSayyad, Y., Ando, M., et al. 2022, *PASJ*, 74, 247
- Anderson, J., Bourque, M., Sahu, K., Sabbit, E., & Viana, A. 2015, A Study of the Time Variability of the PSF in F606W Images taken with the WFC3/UVIS, Tech. rep., *WFC3 2015-08*, Space Telescope Science Institute
- Astropy Collaboration, Price-Whelan, A. M., Sipőcz, B. M., et al. 2018, *AJ*, 156, 123
- Astropy Collaboration, Robitaille, T. P., Tollerud, E. J., et al. 2013, *A&A*, 558, A33
- Behroozi, P., Wechsler, R. H., Hearin, A. P., & Conroy, C. 2019, *MNRAS*, 488, 3143
- Behroozi, P. S., Marchesini, D., Wechsler, R. H., et al. 2013, *ApJL*, 777, L10
- Bezanson, R., van Dokkum, P. G., Tal, T., et al. 2009, *ApJ*, 697, 1290
- Brammer, G. 2019, Grizli: Grism redshift and line analysis software, Astrophysics Source Code Library, ascl:1905.001
- Chiang, Y.-K., Overzier, R., & Gebhardt, K. 2014, *ApJL*, 782, L3
- Civano, F., Elvis, M., Brusa, M., et al. 2012, *ApJS*, 201, 30
- Civano, F., Marchesi, S., Comastri, A., et al. 2016, *ApJ*, 819, 62
- Cooke, K. C., Kartaltepe, J. S., Tyler, K. D., et al. 2019, *ApJ*, 881, 150
- Cutler, S. E., Whitaker, K. E., Mowla, L. A., et al. 2022, *ApJ*, 925, 34
- De Lucia, G., & Blaizot, J. 2007, *MNRAS*, 375, 2
- Dekel, A., Mandelker, N., Bournaud, F., et al. 2022, *MNRAS*, 511, 316
- Duncan, K., Conselice, C. J., Mundy, C., et al. 2019, *ApJ*, 876, 110
- Elmegreen, D. M., Elmegreen, B. G., Whitmore, B. C., et al. 2021, *ApJ*, 908, 121
- Faist, A. L., Schaerer, D., Lemaux, B. C., et al. 2020, *ApJS*, 247, 61
- Fernández, X., Gim, H. B., van Gorkom, J. H., et al. 2016, *ApJL*, 824, L1
- Förster Schreiber, N. M., Shapley, A. E., Genzel, R., et al. 2011, *ApJ*, 739, 45
- Gardner, J. P., Mather, J. C., Clampin, M., et al. 2006, *SSRv*, 123, 485
- Gonzaga, S. 2012, The DrizzlePac Handbook, STScI
- Green, J., Schechter, P., Baltay, C., et al. 2012, arXiv:1208.4012
- Grogin, N. A., Kocevski, D. D., Faber, S. M., et al. 2011, *ApJS*, 197, 35
- Guo, Y., Rafelski, M., Bell, E. F., et al. 2018, *ApJ*, 853, 108
- Hill, A. R., Muzzin, A., Franx, M., et al. 2017, *ApJ*, 837, 147
- Huertas-Company, M., Guo, Y., Fergsburg, O., et al. 2020, *MNRAS*, 499, 814
- Illingworth, G. D., Magee, D., Oesch, P. A., et al. 2013, *ApJS*, 209, 6
- Iovino, A., Petropoulou, V., Scodreggio, M., et al. 2016, *A&A*, 592, A78
- Jacob, J. C., Katz, D. S., Berriman, G. B., et al. 2010, Montage: An Astronomical Image Mosaicking Toolkit, Astrophysics Source Code Library, ascl:1010.036
- Kartaltepe, J., Casey, C. M., Bagley, M., et al. 2021, JWST Proposal, 1, 1727
- Koekemoer, A. M., Aussel, H., Calzetti, D., et al. 2007, *ApJS*, 172, 196
- Koekemoer, A. M., Faber, S. M., Ferguson, H. C., et al. 2011, *ApJS*, 197, 36
- Laureijs, R., Amiaux, J., Arduini, S., et al. 2011, arXiv:1110.3193
- Lawrence, A., Warren, S. J., Almaini, O., et al. 2007, *MNRAS*, 379, 1599
- Le Fèvre, O., Béthermin, M., Faist, A., et al. 2020, *A&A*, 643, A1
- Lee, N., Sanders, D. B., Casey, C. M., et al. 2015, *ApJ*, 801, 80
- Leja, J., Speagle, J. S., Johnson, B. D., et al. 2020, *ApJ*, 893, 111
- Lotz, J. M., Koekemoer, A., Coe, D., et al. 2017, *ApJ*, 837, 97
- Marchesi, S., Civano, F., Elvis, M., et al. 2016, *ApJ*, 817, 34
- Marsan, Z. C., Marchesini, D., Muzzin, A., et al. 2019, *ApJ*, 871, 201
- Marsan, Z. C., Muzzin, A., Marchesini, D., et al. 2022, *ApJ*, 924, 25
- McCracken, H. J., Milvang-Jensen, B., Dunlop, J., et al. 2012, *A&A*, 544, A156
- Momcheva, I. G., van Dokkum, P. G., van der Wel, A., et al. 2017, *PASP*, 129, 015004
- Moster, B. P., Naab, T., & White, S. D. M. 2018, *MNRAS*, 477, 1822
- Mowla, L., van der Wel, A., van Dokkum, P., & Miller, T. B. 2019a, *ApJL*, 872, L13
- Mowla, L. A., van Dokkum, P., Brammer, G. B., et al. 2019b, *ApJ*, 880, 57
- Muzzin, A., Marchesini, D., Stefanon, M., et al. 2013, *ApJS*, 206, 8
- Naab, T., Johansson, P. H., & Ostriker, J. P. 2009, *ApJ*, 699, L178
- Nedkova, K. V., Häußler, B., Marchesini, D., et al. 2021, *MNRAS*, 506, 928
- Oke, J. B., & Gunn, J. E. 1983, *ApJ*, 266, 713
- Pena, T., & Snyder, G. F. 2021, *RNAAS*, 5, 45
- Peng, C. Y., Ho, L. C., Impey, C. D., & Rix, H.-W. 2010, *AJ*, 139, 2097
- Sargent, M. T., Carollo, C. M., Lilly, S. J., et al. 2007, *ApJS*, 172, 434
- Scoville, N., Arnouts, S., Aussel, H., et al. 2013, *ApJS*, 206, 3
- Scoville, N., Aussel, H., Brusa, M., et al. 2007, *ApJS*, 172, 1
- Shipley, H. V., Lange-Vagle, D., Marchesini, D., et al. 2018, *ApJS*, 235, 14
- Skelton, R. E., Whitaker, K. E., Momcheva, I. G., et al. 2014, *ApJS*, 214, 24
- Sorba, R., & Sawicki, M. 2018, *MNRAS*, 476, 1532
- Spergel, D., Gehrels, N., Baltay, C., et al. 2015, arXiv:1503.03757
- Suess, K. A., Kriek, M., Price, S. H., & Barro, G. 2019, *ApJL*, 885, L22
- van der Wel, A., Noeske, K., Bezanson, R., et al. 2016, *ApJS*, 223, 29
- Weaver, J. R., Kauffmann, O. B., Ilbert, O., et al. 2022, *ApJS*, 258, 11
- Whitaker, K. E., Kriek, M., van Dokkum, P. G., et al. 2012a, *ApJ*, 745, 179
- Whitaker, K. E., Labbé, I., van Dokkum, P. G., et al. 2011, *ApJ*, 735, 86
- Whitaker, K. E., van Dokkum, P. G., Brammer, G., & Franx, M. 2012b, *ApJ*, 754, L29
- Williams, R. J., Quadri, R. F., Franx, M., van Dokkum, P., & Labbé, I. 2009, *ApJ*, 691, 1879
- Wuyts, S., Förster Schreiber, N. M., Genzel, R., et al. 2012, *ApJ*, 753, 114
- Xu, C. K., Zhao, Y., Scoville, N., et al. 2012, *ApJ*, 747, 85